scientific reports

OPEN

Tsunami detection by GPS-derived ionospheric total electron content

Mahesh N. Shrivastava[1,2]✉, Ajeet K. Maurya[3], Gabriel Gonzalez[1,2], Poikayil S. Sunil[4], Juan Gonzalez[2,5], Pablo Salazar[1,2] & Rafael Aranguiz[2,5]

To unravel the relationship between earthquake and tsunami using ionospheric total electron content (TEC) changes, we analyzed two Chilean tsunamigenic subduction earthquakes: the 2014 Pisagua M_w 8.1 and the 2015 Illapel M_w 8.3. During the Pisagua earthquake, the TEC changes were detected at the GPS sites located to the north and south of the earthquake epicenter, whereas during the Illapel earthquake, we registered the changes only in the northward direction. Tide-gauge sites mimicked the propagation direction of tsunami waves similar to the TEC change pattern during both earthquakes. The TEC changes were represented by three signals. The initial weaker signal correlated well with Acoustic Rayleigh wave ($AW_{Rayleigh}$), while the following stronger perturbation was interpreted to be caused by Acoustic Gravity wave (AGW_{epi}) and Internal Gravity wave (IGW_{tsuna}) induced by earthquakes and subsequent tsunamis respectively. Inevitably, TEC changes can be utilized to evaluate earthquake occurrence and tsunami propagation within a framework of multi-parameter early warning systems.

Modern geodesy has improved significantly with the extensive use of Global Positioning System (GPS) techniques, allowing the detection of secular variations in the Earth's surface position with unprecedented accuracy[1]. Modern seismology widely uses GPS to understand the nucleation and propagation of earthquake events. It has also been demonstrated that surface deformation related to earthquake and tsunami propagation produce ionospheric changes in the total electron content (TEC)[2–8]. As per the current knowledge of the seismic-ionospheric phenomena studied by many earlier researchers[8–14] suggest observations of three waves, namely acoustic gravity waves at epicenter (AGW_{epi}), internal gravity waves induced by Tsunami (IGW_{tsuna}), and acoustic wave due to seismic Rayleigh wave ($AW_{Rayleigh}$), following the nomenclature introduced by Occhipinti et al.[11]. We remind that AGW_{epi}: in essence the acoustic-gravity wave generated at the epicentral area associated to the vertical displacement of the ground/ocean. It contains a more high-frequency component (0.5–1 Hz). These waves propagate with speed of around 500–1000 m/s and reach the ionosphere ~ 8 min after the earthquake triggering[10,11,14]. These waves frequency is higher than the Brunt Vaisala frequency ~ 2.9 mHz[13]. The IGW_{tsuna} is the internal-gravity wave coupled with the tsunami propagation off-shore. These waves appear in the ionosphere after ~ 40 min of the rupturing. The frequency of these waves is lower than Brunt Vaisala frequency. These waves propagate with a speed of around 200–300 m/s[9,11–18]. The $AW_{Rayleigh}$: is the acoustic wave coupled with the propagation of the seismic Rayleigh wave. These waves have two main frequencies of 3.68 mHz and 4.44 mHz and horizontal speed range from ~ 2.5 to 3.5 km/s[11,19,20]. Though, $AW_{Rayleigh}$ is close to the acoustic wave speed, the corresponding time to reach the ionospheric layers is in the order of 10–15 min. These waves are essentially observed by GNSS-TEC and have been reported in several investigations in the past during the tsunami events[10,11,21,22]. These changes can be detected by GPS instrumentation[2,6,7,9,10,13,14,23]. The identification of these coupled seismo-ionospheric induced signals are essential from a scientific point of view and have been used to improve the tsunami early warning systems (TEWS)[24]. Manta et al.[13] have proposed an empirical method to estimate displaced water volume during the tsunami-genesis by analyzing GPS derived AGW_{epi} and Rakoto et al.[12] proposed a quantitative method to estimate the off-shore tsunami propagation amplitude by analyzing GPS derived IGW_{tsuna}. In the near field, Hébert et al.[25] proposed an integrated technique with buoy GPS, InSAR and pressure gauges anchored on the seafloor in the deep ocean to record tsunami initiation and propagation.

Herein, we correlated the variations of ionospheric TEC from the epicenter towards north and south of the GPS sites located around 1500 km along the Chilean coastal range and the tsunami propagation direction. We used two recent subduction earthquakes (Fig. 1) that occurred in northern Chile as case studies. Both earthquakes (the 2014 Pisagua earthquake M_w 8.1 (Fig. 1B) and the 2015 Illapel earthquake M_w 8.3 (Fig. 1C))

[1]Department of Geological Sciences, Universidad Catolica del Norte, Antofagasta, Chile. [2]National Research Center for Integrated Natural Disaster Management, Santiago, Chile. [3]Department of Physics, Doon University, Dehradun, India. [4]Department of Marine Geology and Geophysics, School of Marine Sciences, Cochin University of Science and Technology, Kochi, India. [5]Department of Civil Engineering, Universidad Catolica de la Santísima Concepcion, Concepcion, Chile. ✉email: mahesh.shrivastava@ucn.cl
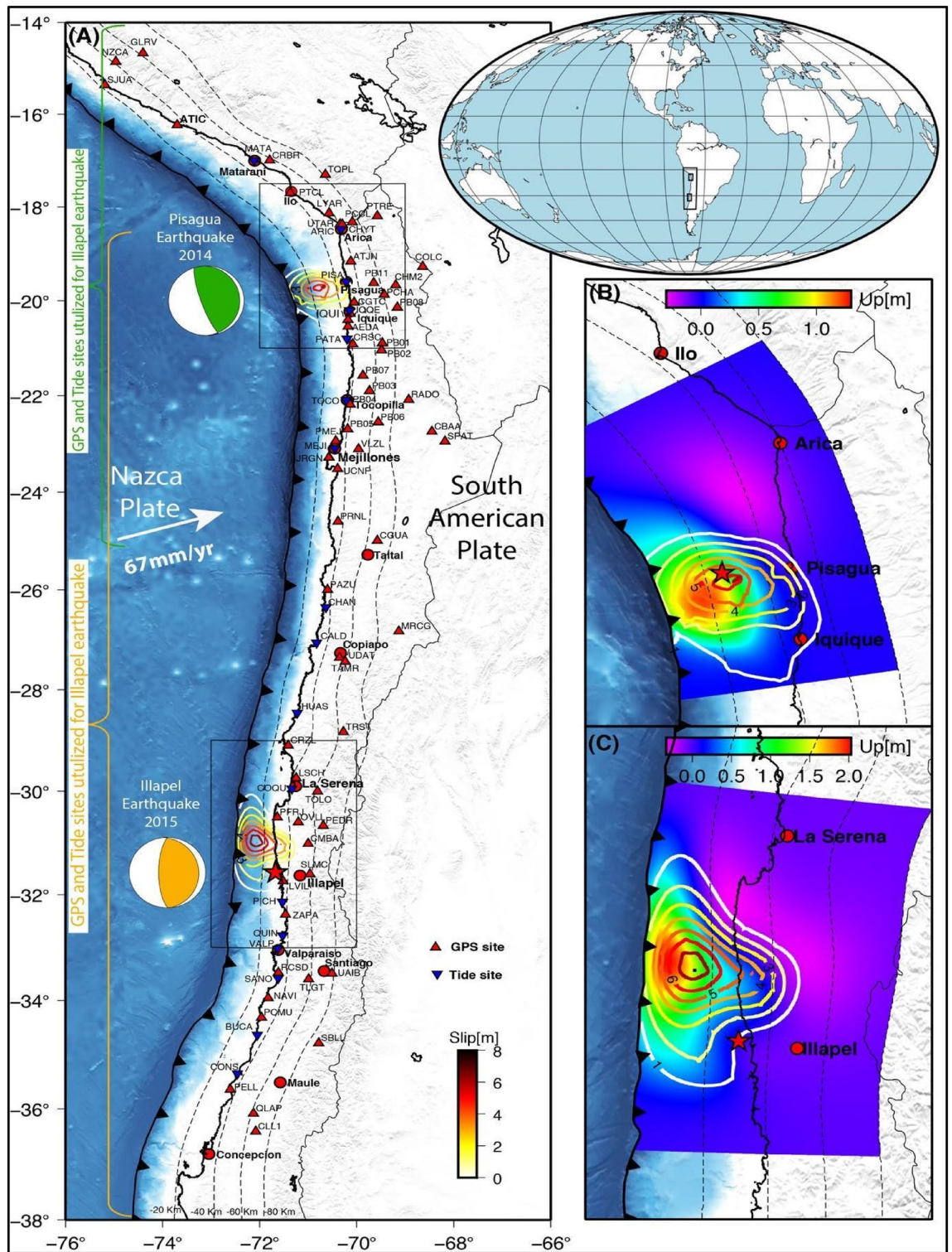
Figure 1. Chilean subduction zone and its tectonic setting. **(A)** The Chilean subduction zone experienced the 2014 Pisagua and the 2015 Illapel earthquakes. The focal mechanism solution of these earthquakes is shown in circles (green for the Pisagua earthquake and orange for the Illapel earthquake). The red triangles show the locations of GPS sites. The blue inverse triangles demonstrate the tide-gauge locations. The coseismic slip is demonstrated with the contour lines. The red stars indicate the earthquake epicenters. The rectangular region represents the area of the vertical deformation study. **(B,C)** The coseismic slip and vertical deformation produced by the Pisagua and Illapel earthquakes.

generated tsunamis, which are described in detail in the literature[26,27]. These two case studies were chosen as they possessed good-quality GPS data and tide-gauge records, allowing us to give a unique opportunity to investigate the components of surface deformation, tsunami propagation, and associated ionospheric TEC perturbations altogether in terms of AGW_{epi}, $AW_{Rayleigh}$ and IGW_{tsuna}.

The Chilean subduction zone forms part of the Ring of Fire, hosting most of the largest earthquakes in the world. In particular, Chile's west coast is characterized by the subduction of the Nazca Plate beneath the South American Plate, resulting in frequent and large megathrust earthquakes[28]. The Nazca Plate subducts east-north-east at a rate of approximately 67 mm/year[29]. Thus, this region yet again experienced two more tsunamigenic earthquakes: the 2014 Pisagua M_w 8.1 and the 2015 Illapel M_w 8.3[26,27,30–34].

Several seismic and aseismic signals are transmitted during earthquakes (e.g., seismic waves, acoustic waves, gravity waves) towards the atmosphere[4]. The ionosphere forms part of the Earth's atmosphere and is located at an altitude of approximately 100–1000 km. It contains ionized gas, called plasma, which influences radio wave propagation[35]. The ionosphere grows and shrinks depending on the energy it absorbs from the top sources (e.g., the sun, interplanetary medium, magnetosphere) and the bottom sources (e.g., mesosphere, stratosphere, troposphere, lithosphere). The lithospheric disturbances are predominantly caused by natural sources (e.g., earthquakes, volcanic eruptions, cryospheric changes)[36–40] or human activity (e.g., nuclear explosions)[41]. The ionosphere is also highly influenced by large-scale tropospheric weather systems[35,42,43], geomagnetic, auroral activity[43–45], earthquakes[3–5,36] and Solar eclipse[46]. During an earthquake, the ionosphere is mainly perturbed by AGW_{epi}, acoustically induced $AW_{Rayleigh}$, and tsunamis provoked IGW_{tsuna}. Since, we observed three signals in the TEC disturbance field (i.e., two related to the earthquake rupture and the one linked to the tsunami propagation), along with the recent investigations[12,13,25] our results from seismic, geodetic and oceanic tide gauge will significantly improve the existing TEWS[24].

Results

Surface deformation. The 2014 Pisagua earthquake M_w 8.1 ruptured a segment of the Nazca-South America subduction zone with the maximum coseismic slip concentrated in a single patch, and a total rupture extending for approximately 100 km along-strike and 130 km downdip[30,31,34,47]. According to the available slip models of the event, the peak coseismic slip of the mainshock occurred at 19.7°S–70.8°W, at a depth of approximately 23 km. The modeled vertical displacement of the Pisagua earthquake inferred from GPS data inversion is shown in Fig. 1B. The maximum uplift of approximately 1.20 m was in the southwestern part of the earthquake epicenter, and the maximum subsidence equaled approximately 0.25 m, being detected north of the epicenter. No vertical deformation occurred in the coastal region south of the main slip region, but minimum subsidence was detected north of the rupture. The 2015 Illapel earthquake M_w 8.3 also had the maximum coseismic slip concentrated in a single patch in the northern and western parts of the earthquake epicenter. The slip extended to the north and south of the main slip region. The interplate contact beneath the coastal region also slightly slipped[30,31,48]. Maximum uplift of approximately 2 m occurred near the trench, and maximum subsidence of 0.2 m was detected to the northeast of the maximum slip region (see Fig. 1C).

Tsunami signature. The Pisagua earthquake M_w 8.1 produced a minor tsunami impact on the coastal area between Matarani (~17° S) and Mejillones (~23° S)[9]. The first wave arrived at Pisagua (~19.5° S) 11.08 min after the mainshock (Table S2). The area located between Arica (~18.5° S) and Patache (~20.8° S) presented the maximum range of wave height (approximately 1.5 m) (Fig. 2). North of Arica, the wave height decreased by almost 68% relative to the Arica tide gauge, whereas south of Patache, the wave height diminished by approximately 49% relative to the Patache tide gauge. On the contrary, the Illapel earthquake M_w 8.3 produced a substantial tsunami impact on the coastal area between Chañaral (~26° S) and Constitución (~35° S). The first wave arrived at Pichidangui (~32° S) 13.70 min after the mainshock (Table S2). The area located between Coquimbo (~30° S) and Valparaíso (~33° S) recorded the maximum range of wave height (over 1.5 m) (Fig. 2). The city of Coquimbo experienced massive flooding and flow height generated by a coastal harbor resonance process[25], this fact is also demonstrated by the tsunami spectrum, which shows large energy at Coquimbo area (Fig. 2). North of Coquimbo, the wave height diminished by approximately 86% relative to the Coquimbo tide gauge, and south of Valparaíso, the wave height decreased by almost 42% relative to the Valparaíso tide gauge.

TEC estimates. TEC over the epicentral region was influenced by surface uplift during both, the Pisagua and Illapel earthquakes (Figs. 1 and 3). During the Pisagua earthquake, 33 GPS sites located along the coastal region in northern Chile and southern Peru detected the ionospheric TEC variations (Fig. 1). The satellite Pseudo-Random Numbers (PRNs) 01, 11, 20, and 23 had sufficient coverage to identify changes in TEC. Three PRNs (13, 17, and 31) partially covered the Pisagua earthquake (Fig. 3A). The remaining TEC change data of the Pisagua earthquake are provided in Supplementary Information Fig. S1. PRNs 01, 11, 20, and 23 recorded significant TEC changes of approximately 1.25 TECU to the north and south of the rupture zone along the coast of northern Chile and southern Peru. Although PRNs 01, 11, and 23 were slightly above the 60° elevation, they could still detect the maximum changes of TEC (1.25 TECU) in the ionosphere (Fig. 3A). Some of the GPS-derived TEC results of Pisagua earthquake have been published by Reddy et al.[49] and He and Heki[50].

As for the Illapel earthquake, we were able to estimate TEC changes from 42 GPS sites. Upon observation that the TEC changes predominated in the northern direction, we selected the GPS sites to the north until Arica and to the south until Concepción. The observed TEC changes were significant (approximately 1.40 TECU) in the northern direction and negligible (approximately 0.35 TECU) in the southern direction. The TEC changes seemed to be unidirectional and not concentric, contrary to the case of the Pisagua earthquake. Astafyeva et al.[51] suggested that properties (e.g., amplitude, waveform etc.) of ionospheric disturbances caused by seismic activity
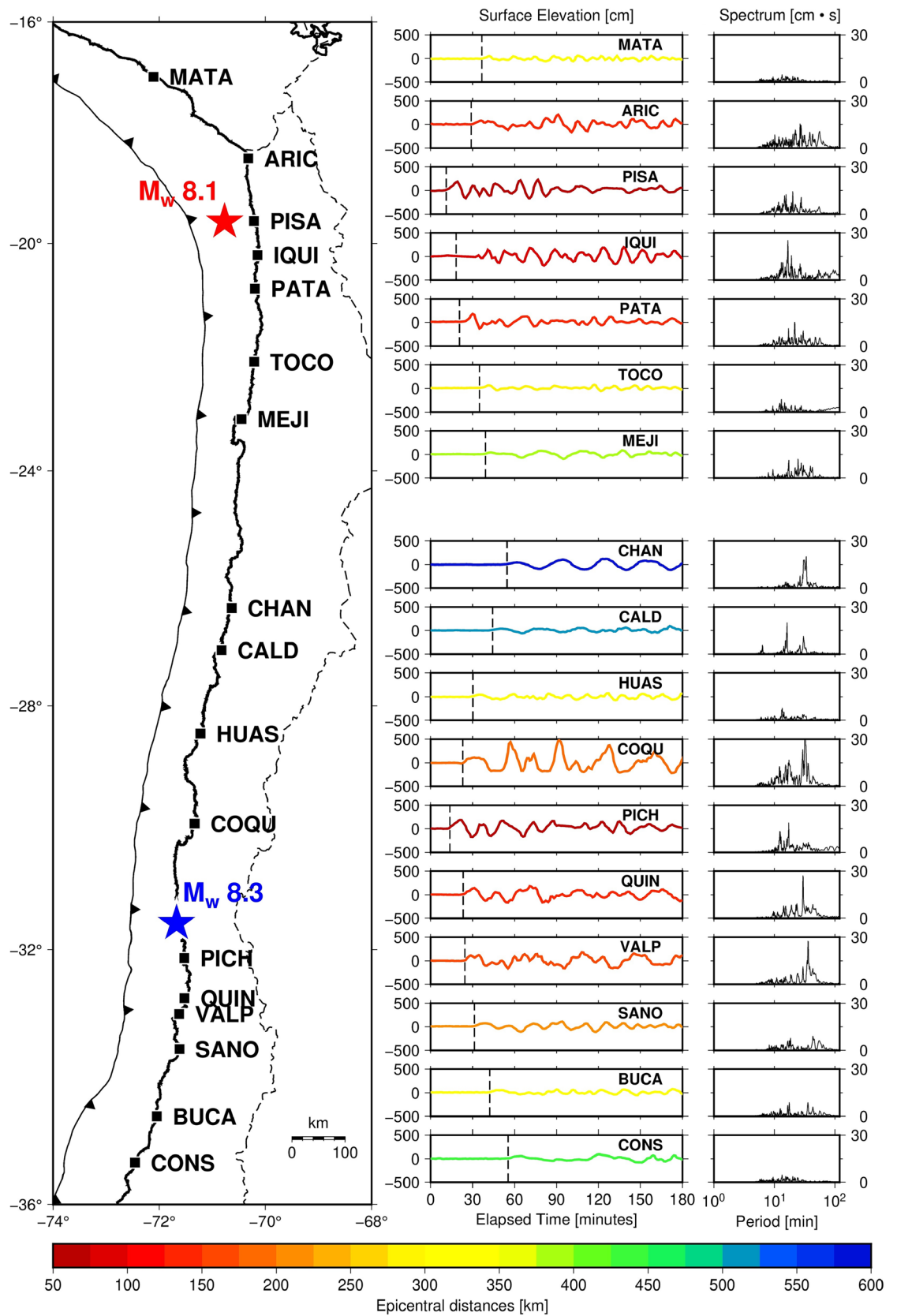
Figure 2. Tide-gauge locations along the Chilean coastal region (left panel). The tsunami waveform for the Pisagua and Illapel earthquakes are shown in central panel. The data were filtered using a zero-phase digital high-pass filter to eliminate signals over 180 min period. The dotted lines show the first arrival of tsunamis to the tide-gauge sites. Tsunami spectra of 24 h of elapsed time are shown in right panel.
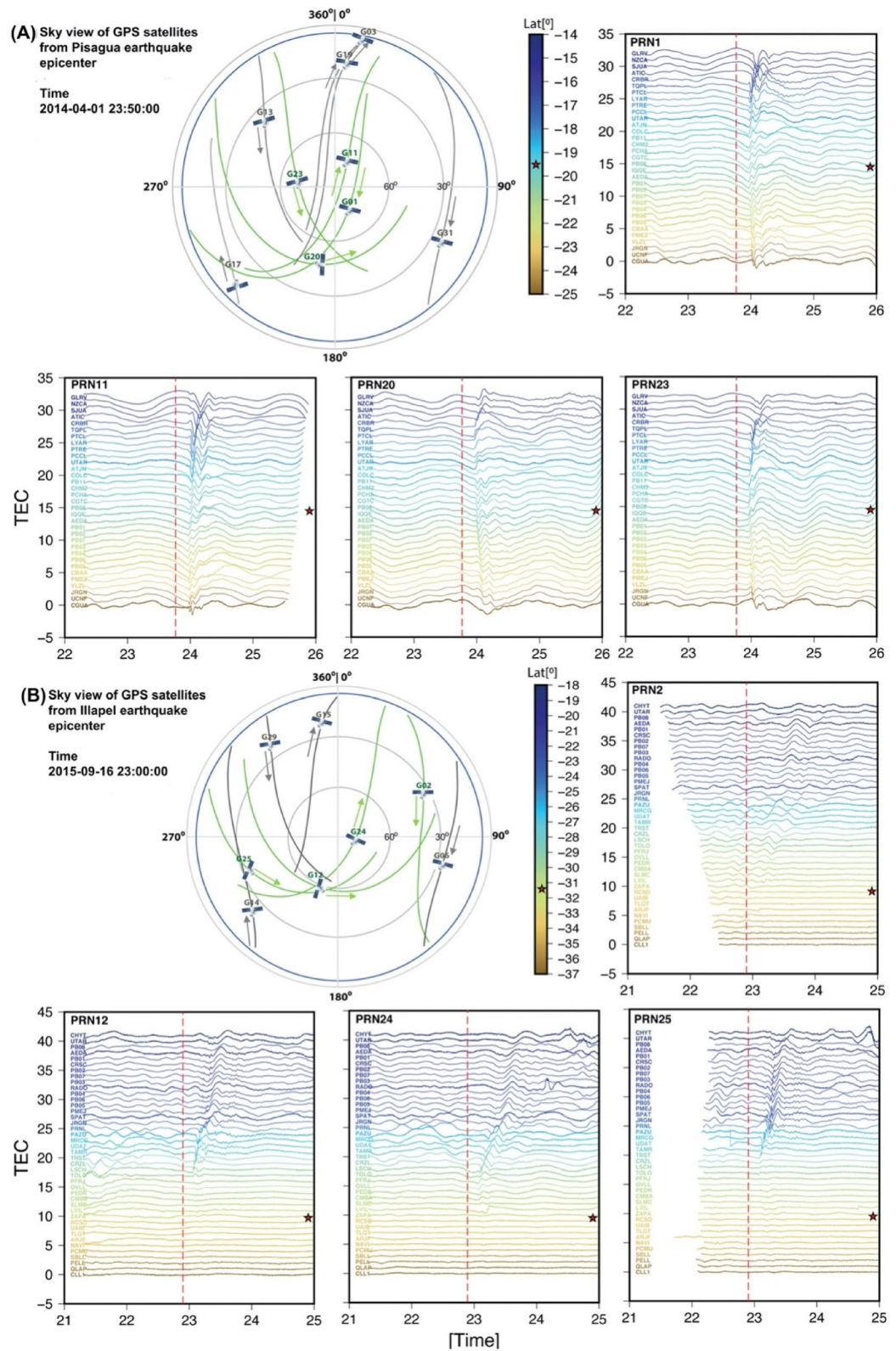
Figure 3. Imaginary sky view of the GPS satellites from the 2014 Pisagua earthquake (**A**) and Pisagua earthquake (**B**) epicenters. The blue circle represents the 20° elevation, which was used as criteria for the utilization of the GPS satellite data. The residual VTEC is presented for PRNs 01, 11, 20, and 23 during the 2014 Pisagua earthquake (**A**) and for PRNs 2, 12, 24, and 25 during the 2015 Illapel earthquake (**B**). The dotted lines mark the time of the earthquakes. The colored lines represent the residual VTEC regarding the locations of GPS latitudinally from north to south. The red stars indicate the latitude of the earthquake epicenters.

are dependent on the observational factors, the current geometry of GNSS-sounding, background ionization and current geomagnetic field. Further, they discussed the effect of earth's magnetic field configuration at the epicenter area, which controls propagation of the co-seismic ionospheric disturbances in the specific direction based on the results of Rolland et al.[10]. Rolland et al.[10] observed minimum change in the co-seismic ionospheric disturbances above and south of the rupture line in the northern hemisphere, whereas minimum changes are observed north of the rupture line in the southern hemisphere. They have discussed the example of $M_w = 8.8$ 2010 offshore Maule Chile earthquake, for which they observed negative initial change in GPS-TEC observations south of rupture line and positive initial change north of rupture line. The presence of unidirectionality in the TEC observations in the case of the Illapel earthquake seems to follow the effect of the geomagnetic field. Furthermore, Reddy et al.[52] and Ravanelli et al.[14] also observed similar unidirectionality in the TEC for Illapel earthquake. The TEC changes detected by PRNs 12 and 25 at elevations ranging from 30° to 60° were characterized by a wavy signal. Other PRNs (2 and 24) did not exhibit any wavy signal (Fig. 3B). The remaining TEC change data of the Illapel earthquake are provided in Supplementary Information Fig. S2.

Changes in TEC were clearly observed during the Pisagua and Illapel earthquakes at different amplitudes. The changes were systemically symmetric at the GPS sites to the north and south of the Pisagua rupture zone. Around 700 s after the earthquake initiation, the TEC changes started to diminish, and within the next 100 s, we detected an increase in the TEC changes. A similar scenario was noted both in the northern and southern directions. Conversely, during the Illapel earthquake, approximately 600 s after the earthquake initiation, we observed a decline and a subsequent increase in the TEC perturbations. The TEC perturbations were observed only to the north of the Illapel rupture and were not recorded in the southern direction (Fig. 3B).

Discussion

The determination of the intensity and amplitude of tsunami and its propagation depends on the initial sea-surface deformation induced by the seabed due to the occurrence of slip along the plate interface, the accompanying water column excitation[53] and bathymetry[54]. The simulation of tsunami propagation in real-time has been attempted by several researchers via automated finite-fault inversion[55,56] and fast numerical propagation and inundation models, such as HySEA[57]. Despite these scientific efforts, there is still a high level of uncertainty and low level of accuracy in the estimation of tsunami hazards[58]. Nowadays, the acquisition of the sea level variation in real-time at the earthquake source is only available for submarine sensors networks[59,60] (e.g., DONET in Japan and NEPTUNE in Canada). In the analyzed area, Chile has an extensive real-time tide gauges network that provides quality information of tsunami coastal propagation. Nevertheless, the tsunami dynamics have to be detected accurately, remotely and redundantly whenever direct observations are not feasible in order to develop a reliable real-time tsunami warning system.

Herein, with the previous works[12,13] and the present analysis, we discuss that space-based geodetic GPS signals can be used to continuously monitor and sense the tsunami signals along with the possibility to estimate amplitude and the volume of displaced water during Tsunami. Thus, enhancing the possibility of tsunami detection in such tectonically active regions as the Chilean subduction zone.

Surface deformation and tsunami propagation. The finite-fault model of the Pisagua and Illapel earthquakes provided details on the vertical deformation caused by both earthquakes (Fig. 1). In the Pisagua region, the maximum vertical uplift was circular and near the epicenter. However, in the Illapel region, the vertical uplift was elliptical and expanded to the north and south from the main uplift peak (Fig. 1). The characteristics of the epicenter and main peak of coseismic slip suggested that, during the Pisagua earthquake, the rupture propagated up-dip towards the west and slightly south. On the contrary, during the Illapel earthquake, the deeply locked zone propagated up-dip and northwest, toward the trench (Fig. 1). The tsunami wave height during the Pisagua earthquake was less than that during the Illapel earthquake (Fig. 2). The Pisagua earthquake-associated tsunami extended to the north and south with almost the same wave height. However, the tsunami associated with the Illapel earthquake propagated only to the north. The finite-fault model[16] suggested that the rupture was initiated near the coast of Illapel and propagated northwestward, presenting a possible reason for the northward tsunami propagation. This explanation is supported by the observed tide-gauge data from the Coquimbo coastal region (Fig. 2). Thus, crustal uplift and tsunami propagation act as bottom sources of ionospheric TEC perturbations.

Relationship between TEC and tsunami propagation. To better understand the effect of two seismic events (i.e., the Pisagua and Illapel earthquakes) on the TEC signature, we performed the wavelet analysis of TEC data. For the analysis, we selected two pairs of GPS, i.e., PRNs 20 and 23 for the Pisagua earthquake and PRNs 24 and 25 for the Illapel earthquake, for all GPS sites. During the Pisagua event, the TEC values presented a perturbation attributed to AGW_{epi} and IGW_{tsuna}. These waves had a frequency of 1–7 mHz at around 700 s after the mainshock and propagated away from the epicenter with a horizontal speed of 500–700 m/s. Subsequently, a low-frequency wave related to IGW_{tsuna} was originated from the tsunami and traveled at a speed of 300 m/s. As for the Illapel earthquake, the TEC signature remained intense and dominant in the northern direction. This signature has also been observed by Reddy et al.[51] and Ravanelli et al.[14]. The spectral analysis of the TEC (Fig. 4A) observed during the Pisagua and Illapel earthquakes revealed the unique characteristics of their AGW_{epi} and IGW_{tsuna}. The TEC traces depicted in the hodochrone of Fig. 5A,B indicate that the satellite coverage was dense enough to assure the detection of AGW_{epi} and IGW_{tsuna}. For identifying the $AW_{Rayleigh}$, we have used band pass filter 3–7 mHz in the TEC data of PRN25. The raw and filtered TEC data are provided in Fig. 4B along with spectrograms. It clearly represents the $AW_{Rayleigh}$ and AGW_{epi} signatures. Further to show the TEC perturbation akin to the $AW_{Rayleigh}$, we provided a hodochrone of PRN12 in Fig. 5C. which clearly portrays the $AW_{Rayleigh}$
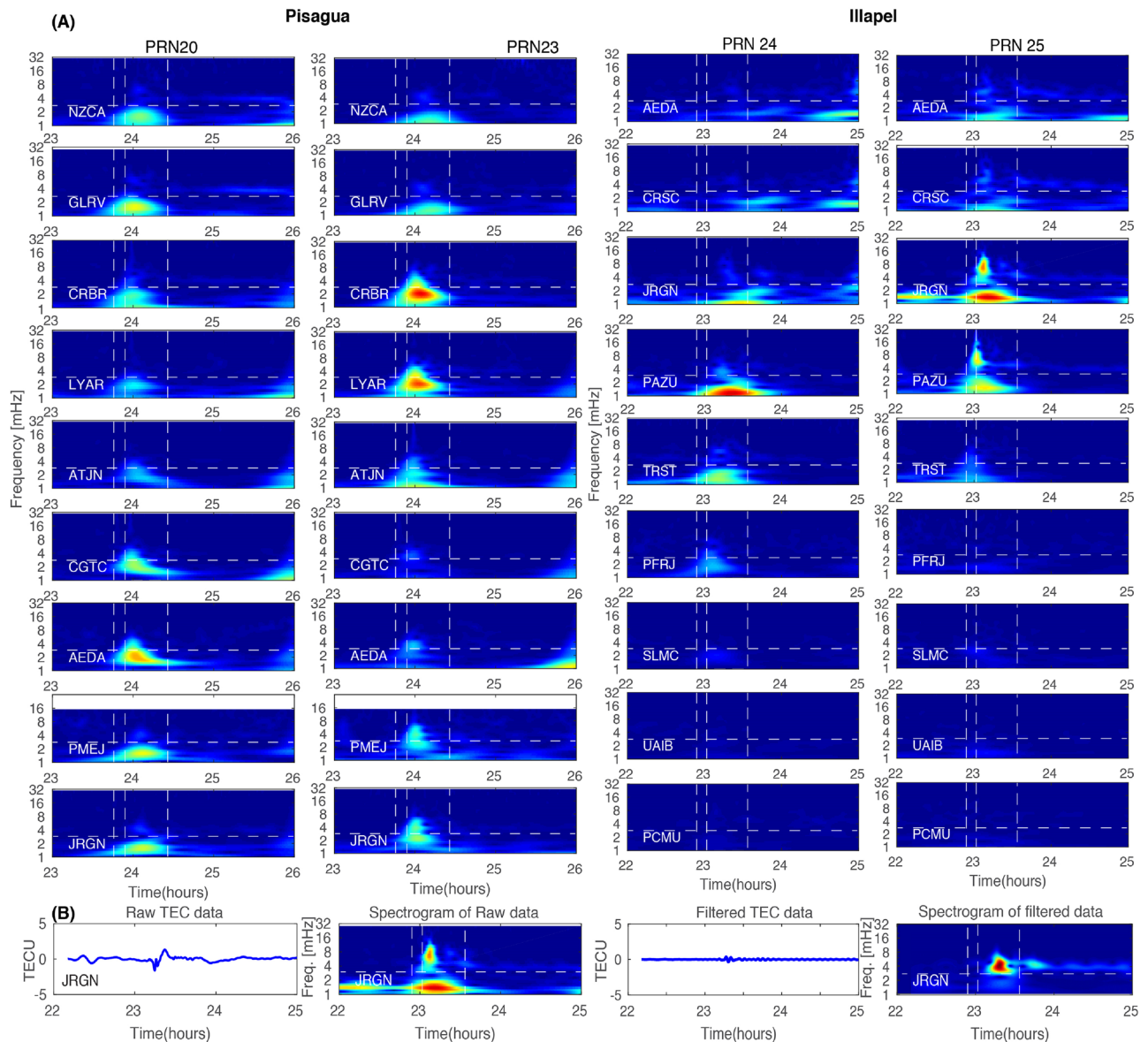
Figure 4. (A) Spectrogram of the residual TEC changes at randomly chosen GPS sites for PRNs 20 and 23 for the Pisagua and PRNs 24 and 25 for the Illapel earthquakes. The first dotted line represents the timing of the earthquakes; the second dotted line demarcates 8 min after the initiation of the earthquakes; and the third dotted line represents 40 min after the initiation of the earthquakes. (B) To identify the $AW_{Rayleigh}$, the raw and filtered TEC of JRGN GPS site of PRN25 along with spectrogram provided.

allied TEC perturbation before AGW_{epi} with a velocity of ~ 2810 m/s in the far field. The remaining TEC traces associated to $AW_{Rayleigh}$, AGW_{epi}, and IGW_{tsuna} are presented in the hodochrone of Supplementary Information Figs. S3 and S4.

As previously proposed, three major mechanisms can explain ionospheric perturbations during earthquakes and associated tsunamis in the form of TEC changes by producing (i) AGW_{epi} waves[6,10,11,14,61,62], (ii) $AW_{Rayleigh}$ by surface Rayleigh waves[10,11,19,20], and (3) IGW_{tsuna} by tsunami waves[9,11–18,63–65]. The propagation of seismo-acoustic waves in the atmosphere and their interactions with the ionospheric plasma are crucial for TEC variations[3–5]. Herein, the TEC perturbation patterns for both earthquakes significantly differed owing to the AGW_{epi} wave propagation directions. The TEC changes were nearly uniform for all satellites during the Pisagua earthquake (Fig. 3) and substantially varied with changing elevation of moving GPS satellites during the Illapel earthquake (Fig. 3).

The AGW_{epi} waves are formed not only due to the uplift of the ocean/land surface but also due to the kinematic uplift of the water column. The water column and crustal uplift depend on the rupture propagation direction and slip appearance during earthquake generation. The TEC changes derived from the GPS signals enable the identification of the rupture propagation direction. The direction of tsunami propagation is affected not only by static slip but also by kinematic slip generation[66]. The crust surface uplift provides direct uplift of the water
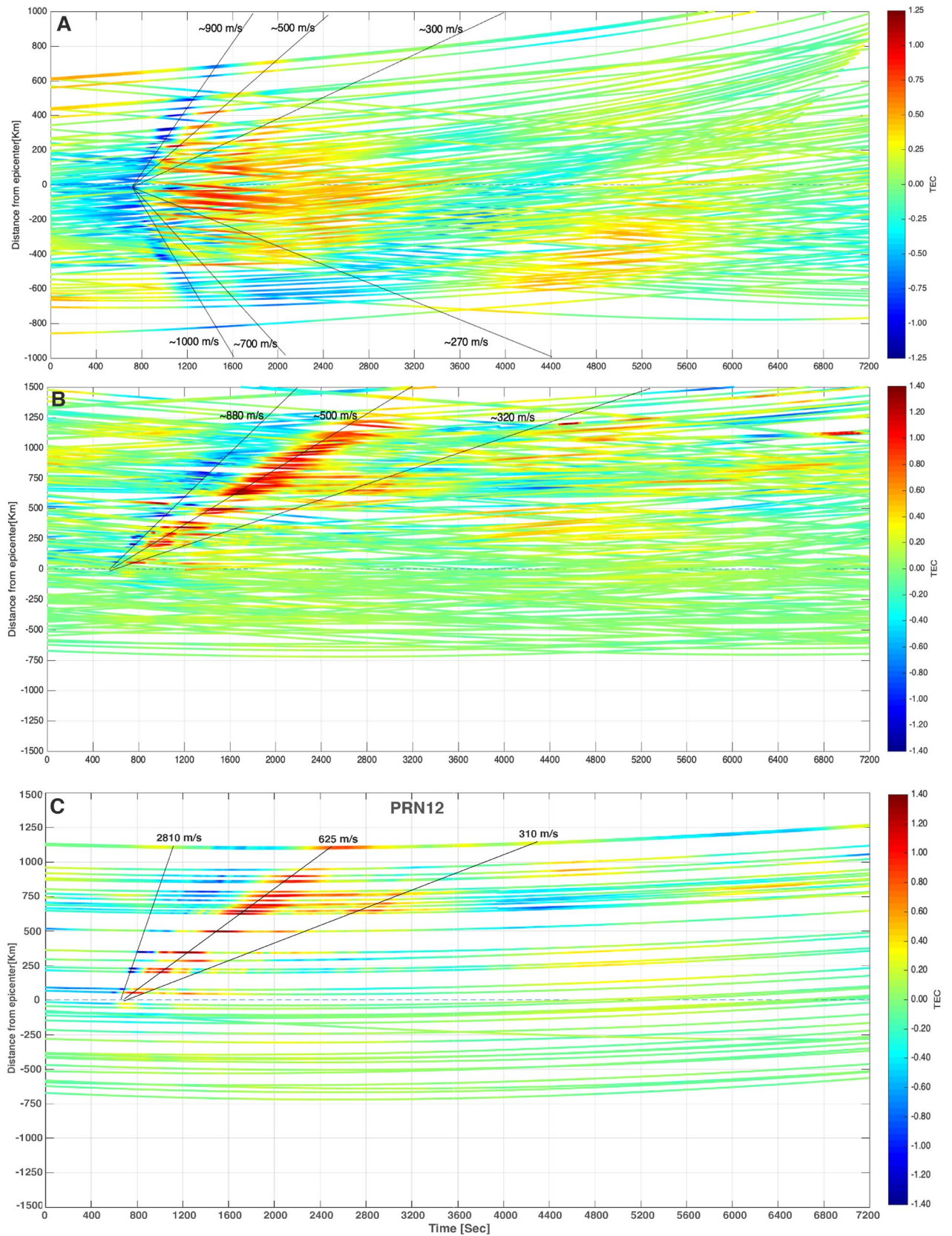
Figure 5. (A) Hodochrone map shows variations in VTEC for PRNs 01, 11, 20, and 23 for GPS sites for two hours duration from 23 to 1 h next day of the Pisagua earthquake on April 1, 2014. (B) Hodochrone plot shows residual VTEC at various GPS sites as a function of time and epicentral distance, as obtained from PRNs 2, 12, 24, and 25 for GPS sites for two hours duration from 22 to 24 h of the Illapel earthquake on September 16, 2016. The positive and negative epicentral distances indicate the northern and southern directions regarding the Illapel earthquake epicenter, respectively. (C) The signature of AW$_{Rayleigh}$ is shown in TEC data of PRN12 in the hodochrone.
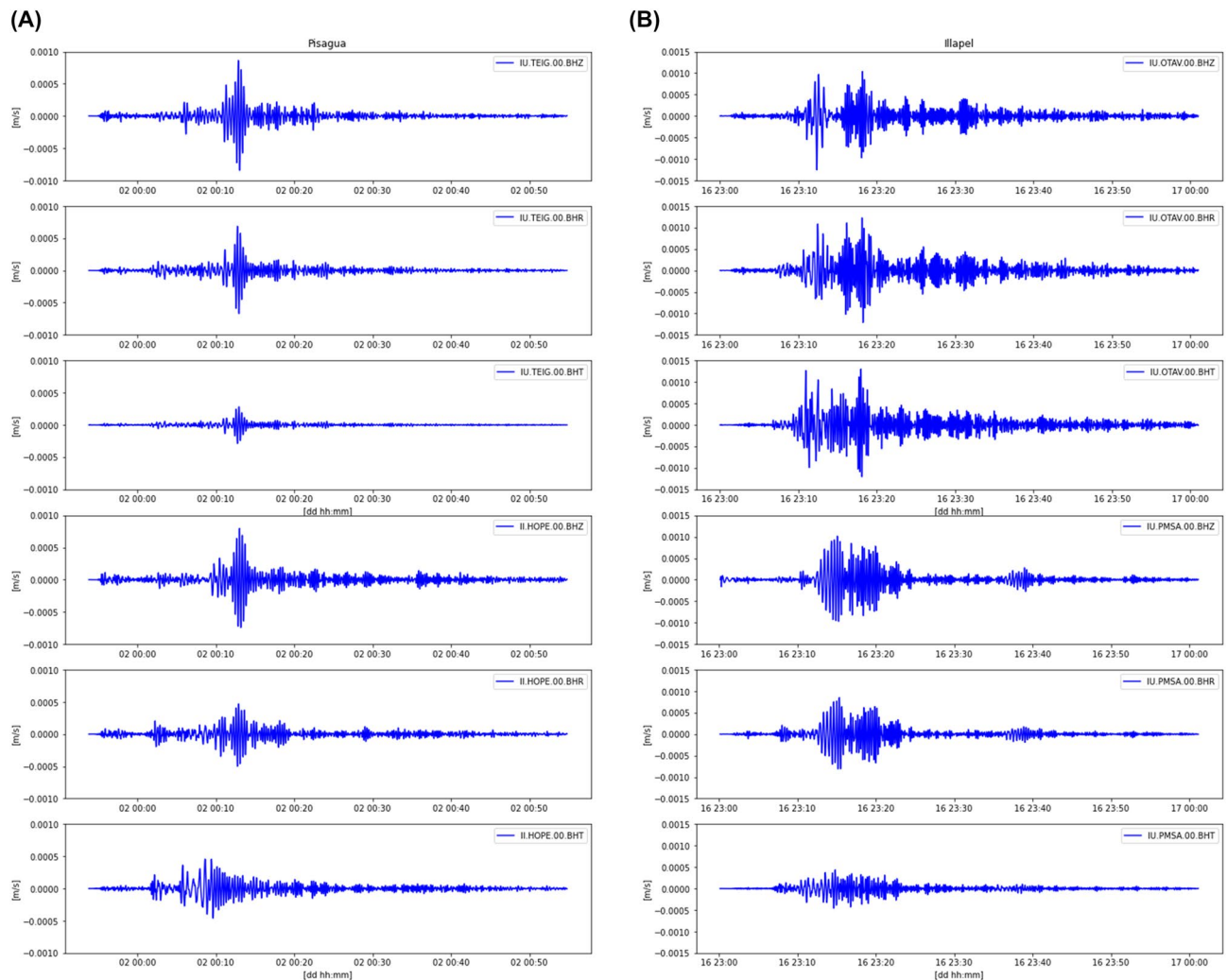
(A)   **(B)**

Figure 6. **(A)** Propagation of Raleigh wave at seismic sites TEIG (to the north) and HOPE (to the south) of the epicenter. These seismic sites are situated approximately 43° away from the Pisagua earthquake epicenter. **(B)** Propagation of Raleigh wave at seismic sites OTAV (to the north) and PMSA (to the south) of the epicenter. These seismic sites are located approximately 33° away from the Illapel earthquake epicenter.

column and subsequent tsunami propagation[67]. The earthquake focal mechanism, the associated direction of rupture propagation, and the earthquake magnitude are equally important in the manifestation of ionospheric responses[21]. Therefore, the TEC changes identified via ground-based GPS sites in the coastal region can be utilized to detect tsunamis in subduction zones in real-time.

Potential of AW$_{Rayleigh}$ waves for tsunami detection. GPS satellites PRNs 02 and 24 passed through elevation angles of approximately 30° and over 70°, respectively (Fig. 3A,B). Both of these satellites detected the same range of perturbations in the TEC signals. However, PRNs 12 and 25 passed between the 30° and 60° elevation angles and detected wavy signals in the TEC perturbation. Rolland et al.[38] suggested that satellites with elevation angles lower than 40° could only provide the efficient detection of AW$_{Rayleigh}$ wave-induced ionospheric waves. However, as shown in Fig. 3, the TEC of PRNs 12 and 25 shows a minor wavy signal that appears before the main TEC perturbation and continues after the inclination in the far field. This wavy signal can be potentially utilized for tsunami detection in tsunami warning systems in the future.

To verify the presence of AW$_{Rayleigh}$ waves in the TEC perturbation during the Pisagua and Illapel earthquakes, we checked the vertical component of seismic Rayleigh waves in the seismic sites situated to the north and south of both rupture zones. The positions of chosen seismic sites are presented in Table S3. Figure 6A,B demonstrates that Rayleigh waves were present in both the Pisagua and Illapel earthquakes. During the Pisagua earthquake, the dispersion of Rayleigh waves was produced in the northern and southern directions, and they had similar energy. The values for the amplitude of the Z and R components from station TEIG (located to the north of the hypocenter) were similar to those from station HOPE (located to the south of the hypocenter) (Fig. 6 and Table S3). A dissimilar pattern in the dispersion of Rayleigh waves was observed during the Illapel earthquake, with different amplitudes of the Z and R components. More intense Rayleigh wave dispersion was detected at

the OTAV station (located to the north of the Illapel hypocenter) rather than at the PMSA station (located to the south of the hypocenter). These observations coincide with the TEC perturbations estimated from the GPS data and indicate that Rayleigh wave propagation during the Illapel earthquake was directed to the north and dispersion to the south. This also explains why Rayleigh wave dispersion to the south was not detected. As a result, the identification of ionospheric perturbations from coastal GPS sites may be a reliable and cost-effective technique to be applied to TEWS. Hence, the GPS-derived TEC methodology can be utilized as it avoids the costs of the new monitoring equipment installation and implementation by using pre-installed GPS sites.

Concluding remarks

Seismic instruments (e.g., ocean buoys, pressure sensors) installed on the ocean bottom and real-time tsunami finite-fault rupture models are currently used to forecast the possible propagation direction of tsunami waves. The research presented herein demonstrates that GPS-derived TEC could also be effectively utilized to improve the existing TEWS. In Chile's coastal region, early tsunami detection is possible via the rapid determination (5–10 min) of changes in TEC using the available GPS sites. Earthquake ruptures significantly displace the ocean surface and create waves (AGW_{epi}, IGW_{tsuna} and $AW_{Rayleigh}$), which reach the ionosphere and cause measurable changes in ionospheric electron density. The joint analysis of seismic events and changes in TEC can substantially improve tsunami detection not only in the Chile subduction zone but also in other tsunami-prone areas worldwide.

Methods and data

Tsunami signals were obtained using remotely accessed GPS data from most Chilean and Peruvian coastal GPS sites. These GPS sites were operated continuously with a sampling rate of 15 s. The propagation direction of the tsunami waves was detected by the tide-gauge sites situated to the north and south of the rupture zone.

Vertical deformation associated with the Pisagua and Illapel earthquakes. The vertical deformation of a megathrust earthquake depends on the coseismic slip pattern and locations in the plate interface. Most of the subduction earthquakes, especially in Chile, occur in the seismo-genic zone 20–60 km deep[69]. The vertical deformations produced during the Pisagua and Illapel earthquakes were modeled following the dislocation theory by Okada[70]. We also used the finite-fault model for the 2014 Pisagua and the 2015 Illapel earthquakes, as suggested by Shrivastava et al.[31,32]. The modeled vertical displacements for the Pisagua and Illapel earthquakes are shown in Fig. 1B,C.

TEC derived from GPS data. The ionosphere serves as a dispersive medium for the propagating GPS signals and reduces the GPS signal velocity. The dispersive potential of TEC can be estimated using the L1 and L2 frequencies of GPS signals. The GPS TEC analysis provides the vertical total electron content (VTEC) estimated by the techniques suggested by Rama Rao et al.[71] and Seemala and Valladares[72]. VTEC is defined as the line integral of the electron density from all GPS satellites visible from each of the receivers above a user-specified elevation cut-off angle (we used 20°). In the GPS system, every satellite transmits signals at two frequencies: $f_1 = 1575.42$ MHz and $f_2 = 1227.60$ MHz.

$$STEC = \frac{2(f_1 f_2)^2}{k\left(f_1^2 - f_2^2\right)}(P_2 - P_1) + \tau^r + \tau^s, \tag{1}$$

where k is the ionosphere refraction and equals 80.62 (m³/s²); P_1 and P_2 are the pseudoranges; and τ^r and τ^s are the differential code biases corresponding to pseudoranges P_1 and P_2.

VTEC (in el/m²) can be computed after Ma and Maruyama[73] as follows:

$$VTEC = STEC \times \cos \chi, \tag{2}$$

where χ is the zenith angle and can be expressed as:

$$\chi = \arcsin\left(\frac{R_E \cos \alpha}{R_E + h}\right). \tag{3}$$

We analyzed VTEC at different sets of GPS stations along the coastal region for two recent Chilean subduction earthquakes: the 2014 Pisagua and the 2015 Illapel. The Pisagua earthquake took place on April 1, 2014, at 23:47 UT in northern Chile, and the Illapel earthquake occurred on September 16, 2015, at 22:54 UT in central Chile. For TEC analysis, we used the GPS site data (Table S1) and considered the satellite data up to the 20° elevation. During the Pisagua earthquake (from its epicenter to the 20° elevation in the sky), seven satellites were available, including PRNs 01, 11, 13, 19, 20, 23, and 31. Within the first 10 min after the earthquake initiation, PRN 19 went below the 20° elevation, and no other satellite vehicle appeared in the 20° elevation region. However, satellite PRN 17 appeared 20 min later. Therefore, we utilized seven PRNs (i.e., 01, 11, 13, 17, 20, 23, and 31) for VTEC analysis. To detect changes in VTEC associated with the Pisagua earthquake, the VTEC data were analyzed 2 h before and 2 h after the earthquake. As the Pisagua earthquake occurred at 23:47 UT, in order to obtain complete coverage of 2 h after the earthquake, we added the TEC data for April 1–2, 2014. Thus, we chose PRNs 01, 11, 20, and 23, which provided good coverage from 22:00 UT to 02:00 UT for April 1–2, 2014.

A similar analysis was performed for the Illapel earthquake. Our choice of GPS stations is shown in Table S1. During the Illapel earthquake (from its epicenter to the 20° elevation in the sky), six satellites were available, including PRNs 02, 06, 12, 15, 24, and 25. Within the first 10 min after the earthquake initiation, PRN 15 went

below the 20° elevation, whereas PRNs 14 and 29 went above the 20° elevation region. Therefore, seven PRNs (i.e., 02, 06, 12, 14, 24, 25, and 29) were utilized for TEC analysis. PRNs 02, 12, 24, and 25 were chosen as they fully covered the earthquake timing (at 22:54 UT) from 21:00 UT to 24:00 UT.

To better visualize the effect of the earthquake and tsunami on the TEC data, we estimated differential VTEC (DVTEC) by fitting a 7th order polynomial to the VTEC data for each station, following Ozeki and Heki[74] and Lay et al.[75]. The 7th order polynomial was chosen because it provides the best fit with the VTEC data. This method proved to be effective and revealed the earthquake and tsunami effects, allowing us to remove only the diurnal periodic variations and leave the remaining signals with TEC changes. The final TEC changes associated with the Pisagua and Illapel earthquakes are illustrated in Fig. 3A,B, respectively.

Sea-level record of tsunamis associated with the Pisagua and Illapel earthquakes. The sea-level records of the 2014 Pisagua and the 2015 Illapel earthquakes were extracted from the coastal tide-gauge network [http://www.ioc-sealevelmonitoring.org]. The tsunami records were processed through a zero-phase digital high-pass filter to eliminate signals over a 3-h period to filter out tidal variations[76]. This value is selected based on the results of Bai et al.[77], thus only shelf and bay modes may be identified. As a matter of fact, previous results from Catalán et al.[24] showed that most important resonant modes are lower than 120 min in northern Chile. Moreover, the tsunami spectra were computed from 24 h of elapsed time once arrival.

Detection of AW$_{Rayleigh}$ waves using Pisagua and Illapel seismic waveforms. The seismic wave-forms and instrumental responses were obtained from the IRIS website (IRISDMC, http://ds.iris.edu/wilber3/find_event). The metadata for the selected stations is provided in Supplementary Information Table S3. To detect the Pisagua and Illapel AW$_{Rayleigh}$ from the seismic waveform data, we considered a spectral bandwidth of 0.02–0.2 Hz. We applied the 10th order Butterworth bandpass filter to remove the instrumental response between the frequencies mentioned above. The corrected and filtered waveforms were rotated to the ZNE coordinate system (Z, North, East). To analyze the AW$_{Rayleigh}$ amplitudes with more precision, a new rotation was performed from the NE (northeast) to RT (radial transverse) directions. The AW$_{Rayleigh}$ were principally analyzed in the Z (vertical) and R (radial) directions, and the amplitudes were in velocity units (m/s).

References

1. Dong, D. et al. Anatomy of apparent seasonal variations from GPS-derived site position time series. *J. Geophys. Res.* **107**(B4), ETG 9-1 (2002).
2. Galvan, D. A. et al. The 2009 Samoa and 2010 Chile tsunamis as observed in the ionosphere using GPS total electron content. *J. Geophys. Res.* **116**(6), 1–21 (2011).
3. Kelley, M. C., Livingston, R. & McCready, M. Large amplitude thermospheric oscillations induced by an earthquake. *Geophys. Res. Lett.* **12**(9), 577–580 (1985).
4. Calais, E. & Minster, J. B. GPS detection of ionospheric perturbations following the January 17, 1994, Northridge earthquake. *Geophys. Res. Lett.* **22**(9), 1045–1048 (1995).
5. Artru, J., Lognonné, P. & Blanc, E. Normal modes modelling of post-seismic ionospheric oscillations. *Geophys. Res. Lett.* **28**(4), 697–700 (2001).
6. Mannucci, A. J., Wilson, B. D. & Edwards, C. D. *A New Method for Monitoring the Earth's Ionospheric Total Electron Content Using the GPS Global Network* (Jet Propulsion Laboratory, 1993).
7. Mannucci, A. J. et al. A global mapping technique for GPS-derived ionospheric total electron content measurements. *Radio Sci.* **33**(3), 565–582 (1998).
8. Occhipinti, G. The seismology of the planet Mongo: The 2015 ionospheric seismology review. *Subduct. Dyn.* **211**, 169–182 (2016).
9. Rolland, L. The 29 September 2009 Samoan tsunami in the ionosphere detected offshore Hawaii. *Geophys. Res. Lett.* **37**, L17191 (2010).
10. Rolland, L. M., Lognonné, P. & Munekane, H. Detection and modeling of Rayleigh wave induced patterns in the ionosphere. *J. Geophys. Res.* https://doi.org/10.1029/2010JA016060 (2011).
11. Occhipinti, G. et al. From Sumatra 2004 to Tohoku-Oki 2011: The systematic GPS detection of the ionospheric signature induced by tsunamigenic earthquakes. *J. Geophys. Res.* **118**(6), 3626–3636 (2013).
12. Rakoto, V. et al. Tsunami wave height estimation from GPS-derived ionospheric data. *J. Geophys. Res.* **123**(5), 4329–4348 (2018).
13. Manta, F. et al. Rapid identification of tsunamigenic earthquakes using GNSS ionospheric sounding. *Sci. Rep.* **10**(1), 1–10 (2020).
14. Ravanelli, M. et al. GNSS total variometric approach: First demonstration of a tool for real-time tsunami genesis estimation. *Sci. Rep.* **11**(1), 1–12 (2021).
15. Makela, J. J. et al. Imaging and modeling the ionospheric airglow response over Hawaii to the tsunami generated by the Tohoku earthquake of 11 March 2011. *Geophys. Res. Lett.* https://doi.org/10.1029/2011GL047860 (2011).
16. Occhipinti, G. et al. Three-dimensional numerical modeling of tsunami-related internal gravity waves in the Hawaiian atmosphere. *Earth Planets Space* **63**(7), 847–851 (2011).
17. Grawe, M. A. & Makela, J. J. Observation of tsunami-generated ionospheric signatures over Hawaii caused by the 16 September 2015 Illapel earthquake. *J. Geophys. Res.* **122**(1), 1128–1136 (2017).
18. Occhipinti, G. et al. Three-dimensional waveform modeling of ionospheric signature induced by the 2004 Sumatra tsunami. *Geophys. Res. Lett.* https://doi.org/10.1029/2006GL026865 (2006).
19. Reddy, C. D. & Seemala, G. K. Two-mode ionospheric response and Rayleigh wave group velocity distribution reckoned from GPS measurement following Mw 7.8 Nepal earthquake on 25 April 2015. *J. Geophys. Res.* **120**(8), 7049–7059 (2015).
20. Catherine, J. K. et al. Ionospheric disturbances triggered by the 25 April, 2015 M7.8 Gorkha earthquake, Nepal: Constraints from GPS TEC measurements. *J. Asian Earth Sci.* **133**, 80–88 (2017).
21. Lognonne, P., Clévédé, E. & Kanamori, H. Computation of seismograms and atmospheric oscillations by normal-mode summation for a spherical earth model with realistic atmosphere. *Geophys. J. Int.* **135**(2), 388–406 (1998).
22. Occhipinti, G. et al. Nostradamus: The radar that wanted to be a seismometer. *Geophys. Res. Lett* **37**, 18 (2010).

23. Bagiya, M. S. *et al.* Efficiency of coseismic ionospheric perturbations in identifying crustal deformation pattern: Case study based on Mw 7.3 May Nepal 2015 earthquake. *J. Geophys. Res.* **122**(6), 6849–6857 (2017).
24. Lognonné, P. *et al.* Ground-based GPS imaging of ionospheric post-seismic signal. *Planet Space Sci.* **54**(5), 528–540 (2006).
25. Hébert, H. *et al.* Contributions of space missions to better tsunami science: Observations models and warnings. *Surv. Geophys.* **41**(6), 1535–1581 (2020).
26. Catalán, P. A. *et al.* The 1 April 2014 Pisagua tsunami: Observations and modeling. *Geophys. Res. Lett.* **42**(8), 2918–2925 (2015).
27. Aránguiz, R. *et al.* The 16 September 2015 Chile Tsunami from the post-tsunami survey and numerical modeling perspectives. *Pure Appl. Geophys.* **173**(2), 333–348 (2016).
28. Lay, T. & Kanamori, H. An asperity model of large earthquake. In *Earthquake Prediction: An International Review Maurice Ewing Series* (eds Simpson, D. W. & Richards, P. G.) 579–592 (AGU, Washington, D.C., 1981).
29. Métois, M., Socquet, A. & Vigny, C. Interseismic coupling, segmentation and mechanical behavior of the central Chile subduction zone. *J. Geophys. Res.* **117**(3), 1–16 (2012).
30. Ruiz, S. *et al.* Intense foreshocks and a slow slip event preceded the 2014 Iquique Mw 8.1 earthquake. *Science* **345**(6201), 1165–1169 (2014).
31. Schurr, B. *et al.* Gradual unlocking of plate boundary controlled initiation of the 2014 iquique earthquake. *Nature* **512**(7514), 299–302 (2014).
32. Ruiz, S. *et al.* The seismic sequence of the 16 September 2015 M w 8.3 Illapel, Chile, earthquake. *Seismol. Res. Lett.* **87**(4), 789–799 (2016).
33. Shrivastava, M. N. *et al.* Coseismic slip and afterslip of the 2015 Mw 8.3 Illapel (Chile) earthquake determined from continuous GPS data. *Geophys. Res. Lett.* **43**(20), 10710–10719 (2016).
34. Shrivastava, M. N. *et al.* Earthquake segmentation in northern Chile correlates with curved plate geometry. *Sci. Rep.* **9**(1), 1–10 (2019).
35. Kelley, M. C. In situ ionospheric observations of severe weather-related gravity waves and associated small-scale plasma structure. *J. Geophys. Res.* **102**(A1), 329–335 (1997).
36. Maurya, A. K. *et al.* Sub-ionospheric very low frequency perturbations associated with the 12 May 2008 M = 7.9 Wenchuan earthquake. *Nat. Hazards Earth Syst. Sci.* **13**, 2331–2336 (2013).
37. Maurya, A. K. *et al.* The 25 April 2015 Nepal Earthquake: Investigation of precursor in VLF subionospheric signal. *J. Geophys. Res.* **121**(10), 10–403 (2016).
38. Lean, J. L. *et al.* Ionospheric total electron content: Spatial patterns of variability. *J. Geophys. Res.* **121**(10), 10–367 (2016).
39. Shults, K., Astafyeva, E. & Adourian, S. Ionospheric detection and localization of volcano eruptions on the example of the April 2015 Calbuco events. *J. Geophys. Res.* **121**(10), 10–303 (2016).
40. Manta, F. *et al.* Correlation between GNSS-TEC and eruption magnitude supports the use of ionospheric sensing to complement volcanic hazard assessment. *J. Geophys. Res.* https://doi.org/10.1029/2020JB020726 (2019).
41. Row, R. V. Acoustic-gravity waves in the upper atmosphere due to a nuclear detonation and an earthquake. *J. Geophys. Res.* **72**(5), 1599–1610 (1967).
42. Hung, R. J., Phan, T. & Smith, R. E. Observation of gravity waves during the extreme tornado outbreak of 3 April 1974. *J. Atmos. Terrest. Phys.* **40**(7), 831–843 (1978).
43. Xiao, Z. *et al.* Morphological features of ionospheric response to typhoon. *J. Geophys. Res.* **112**, A04304 (2007).
44. Richmond, A. D. & Matsushita, S. Thermospheric response to a magnetic substorm. *J. Geophys. Res.* **80**(19), 2839–2850 (1975).
45. Nicolls, M. J. *et al.* Imaging the structure of a large-scale TID using ISR and TEC data. *Geophys. Res. Lett.* **31**(9), L09812 (2004).
46. Maurya, A. K., Shrivastava, M. N. & Kumar, K. N. Ionospheric monitoring with the Chilean GPS eyeball during the South American total solar eclipse on 2nd July 2019. *Sci. Rep.* **10**(1), 1–10 (2020).
47. Duputel, Z. *et al.* The Iquique earthquake sequence of April 2014: Bayesian modeling accounting for prediction uncertainty. *Geophys. Res. Lett.* **42**(19), 7949–7957 (2015).
48. Tilmann, F. *et al.* The 2015 Illapel earthquake, central Chile: A type case for a characteristic earthquake?. *Geophys. Res. Lett.* **43**(2), 574–583 (2016).
49. Reddy, C. D. *et al.* Near-field co-seismic ionospheric response due to the northern Chile Mw 8.1 Pisagua earthquake on April 1, 2014 from GPS observations. *J. Atmos. Solar-Terrest. Phys.* **134**, 1–8 (2015).
50. He, L. & Heki, K. Three-dimensional distribution of ionospheric anomalies prior to three large earthquakes in Chile. *Geophys. Res. Lett.* **43**(14), 7287–7293 (2016).
51. Astafyeva, E. Ionospheric detection of natural hazards. *Rev. Geophys.* **57**(4), 1265–1288 (2019).
52. Reddy, C. D. *et al.* Ionospheric plasma response to M w 8.3 Chile Illapel Earthquake on September 16, 2015. In *The Chile-2015 (Illapel) Earthquake and Tsunami* 145–155 (Birkhäuser, 2017).
53. Satake, K. & Atwater, B. F. Long-term perspectives on giant earthquakes and tsunamis at subduction zones. *Annu. Rev. Earth Planet. Sci.* **35**, 349–374 (2007).
54. Geist, E. L. Phenomenology of tsunamis: Statistical properties from generation to runup. *Adv. Geophys.* **51**, 107–169 (2009).
55. Melgar, D. & Bock, Y. Near-field tsunami models with rapid earthquake source inversions from land- and ocean-based observations: The potential for forecast and warning. *J. Geophys. Res. Solid Earth* **118**(11), 5939–5955 (2013).
56. Benavente, R., Cummins, P. R. & Dettmer, J. Rapid automated W-phase slip inversion for the Illapel great earthquake (2015, Mw = 8.3). *Geophys. Res. Lett.* **43**(5), 1910–1917 (2016).
57. Macías, J. *et al.* Performance benchmarking of tsunami-HySEA model for NTHMP's inundation mapping activities. *Pure Appl. Geophys.* **174**(8), 3147–3183 (2017).
58. Cienfuegos, R. *et al.* What can we do to forecast tsunami hazards in the near field given large epistemic uncertainty in rapid seismic source inversions?. *Geophys. Res. Lett.* **45**(10), 4944–4955 (2018).
59. Aoi, S. *et al.* MOWLAS: NIED observation network for earthquake, tsunami and volcano. *Earth Planets Space* **72**, 1–31 (2020).
60. Rabinovich, A. B. & Eblé, M. C. Deep-ocean measurements of tsunami waves. *Pure Appl. Geophys.* **172**(12), 3281–3312 (2015).
61. Calais, E. *et al.* Ionospheric signature of surface mine blasts from Global Positioning System measurements. *Geophys. J. Int.* **132**(1), 191–202 (2018).
62. Heki, K. & Ping, J. Directivity and apparent velocity of the coseismic ionospheric disturbances observed with a dense GPS array. *Earth Planet. Sci. Lett.* **236**(3–4), 845–855 (2005).
63. Tulasi Ram, S. *et al.* Coseismic traveling ionospheric disturbances during the Mw 7.8 Gorkha, Nepal, Earthquake on 25 April 2015 from ground and spaceborne observations. *J. Geophys. Res. Space Phys.* **122**(10), 10–669 (2017).
64. Maruyama, T. *et al.* Ionospheric multiple stratifications and irregularities induced by the 2011 off the Pacific coast of Tohoku Earthquake. *Earth Planets Space* **63**(7), 869–873 (2011).
65. Tsai, H. F. *et al.* Tracking the epicenter and the tsunami origin with GPS ionosphere observation. *Earth Planets Space* **63**(7), 63 (2011).
66. Ulrich, T. *et al.* Coupled, physics-based modeling reveals earthquake displacements are critical to the 2018 Palu, Sulawesi Tsunami. *Pure Appl. Geophys.* **176**(10), 4069–4109 (2019).
67. Melgar, D., Bock, Y. & Crowell, B. W. Real-time centroid moment tensor determination for large earthquakes from local and regional displacement records. *Geophys. J. Int.* **188**(2), 703–718 (2012).
68. Wessel, P. *et al.* Generic mapping tools: Improved version released. *Eos Trans. Am. Geophys. Union* **94**, 409–410 (2013).

69. Chlieh, M. *et al.* Interseismic coupling and seismic potential along the Central Andes subduction zone. *J. Geophys. Res. Solid Earth* **116**(12), 1–21 (2011).
70. Okada, Y. Surface deformation due to shear and tensile faults in a half-space. *Bull. Seismological Soc. Am.* **75**(4), 1135–1154 (1985).
71. Rama Rao, P. V. S. *et al.* Temporal and spatial variations in TEC using simultaneous measurements from the Indian GPS network of receivers during the low solar activity period of 2004–2005. *Ann. Geophys.* **24**(12), 3279–3292 (2006).
72. Seemala, G. K. & Valladares, C. E. Statistics of total electron content depletions observed over the south American continent for the year 2008. *Radio Sci.* **46**, 5 (2011).
73. Ma, G. & Maruyama, T. Derivation of TEC and estimation of instrumental biases from GEONET in Japan. *Ann. Geophys.* **21**, 2083–2093 (2003).
74. Ozeki, M. & Heki, K. Ionospheric Holes Made by Ballistic Missiles from North Korea Detected with a Japanese Dense GPS Array. *J. Geophys. Res.* **115**(9), 1–11 (2010).
75. Lay, E. H., Shao, X. M. & Carrano, C. S. Variation in total electron content above large thunderstorms. *Geophys. Res. Lett.* **40**(10), 1945–1949 (2013).
76. Aranguiz, R. *et al.* Tsunami resonance and spatial pattern of natural oscillation modes with multiple resonators. *J. Geophys. Res.* **124**(11), 7797–7816 (2019).
77. Bai, Y., Yamazaki, Y. & Cheung, K. F. Interconnection of multi-scale standing waves across the Pacific Basin from the 2011 Tohoku Tsunami. *Ocean Model* **92**, 183–197 (2015).

Acknowledgements

Author contributions

M.N.S. and A.K.M. initiated this work by starting the GPS data analysis to determine TEC perturbations. M.N.S., A.K.M., G.G., P.S.S., and R.A. contributed to the interpretation of TEC perturbation results. P.S. conducted the Rayleigh wave analysis using seismic waveform data. J.G. and R.A. analyzed the patterns of tsunami wave propagation using the tide-gauge data. All authors actively participated in the scientific discussions and preparation of the manuscript.

Competing interests

The authors declare no competing interests.

Additional information

Supplementary Information The online version contains supplementary material available at https://doi.org/10.1038/s41598-021-92479-3.

Correspondence and requests for materials should be addressed to M.N.S.

Reprints and permissions information is available at www.nature.com/reprints.

Publisher's note Springer Nature remains neutral with regard to jurisdictional claims in published maps and institutional affiliations.